

## Article

# Investigation of the Effect of Milling Duration on a Ce-Gd Doped Zirconolite Phase Assemblage Synthesised by Hot Isostatic Pressing

Merve Kuman, Laura J. Gardner, Lewis R. Blackburn, Martin C. Stennett, Neil C. Hyatt and Claire L. Corkhill \*

NucleUS Immobilisation Science Laboratory, Department of Materials Science and Engineering, University of Sheffield, Sir Robert Hadfield Building, Mappin Street, Sheffield S1 3JD, UK

\* Correspondence: c.corkhill@sheffield.ac.uk

**Abstract:** Zirconolite is a candidate ceramic wasteform under consideration for the immobilisation of the UK civil PuO<sub>2</sub> inventory. In the present work, a baseline dual-substituted zirconolite with the target composition (Ca<sub>0.783</sub>Gd<sub>0.017</sub>Ce<sub>0.2</sub>)(Zr<sub>0.883</sub>Gd<sub>0.017</sub>Ce<sub>0.1</sub>)(Ti<sub>1.6</sub>Al<sub>0.4</sub>)O<sub>7</sub> was fabricated by hot isostatic pressing (HIPing). In order to optimise the microstructure properties and improve the obtained yield of the zirconolite phase, a range of planetary ball milling parameters were investigated prior to consolidation by HIP. This included milling the batched oxide precursors at 400 rpm for up to 120 min, the pre-milling of CeO<sub>2</sub> (PuO<sub>2</sub> surrogate) to reduce the particle size and using a CeO<sub>2</sub> source with finer particle size (<5 μm). The HIPed zirconolite product consisted of both zirconolite-2M and zirconolite-3T polytypes in varying proportions; however, an additional perovskite phase was obtained in varying quantities as a secondary phase. Ce L<sub>3</sub>-edge X-ray absorption spectroscopy was utilised to determine the Ce oxidation state. In this study, the ideal milling parameter for the fabrication of zirconolite waste forms was defined as 60 min at 400 rpm.

**Keywords:** zirconolite; plutonium; HIP; XRD; SEM; XANES



**Citation:** Kuman, M.; Gardner, L.J.; Blackburn, L.R.; Stennett, M.C.; Hyatt, N.C.; Corkhill, C.L.

Investigation of the Effect of Milling Duration on a Ce-Gd Doped Zirconolite Phase Assemblage Synthesised by Hot Isostatic Pressing. *Ceramics* **2023**, *6*, 707–716. <https://doi.org/10.3390/ceramics6010043>

Academic Editor:  
Lakshminarayana Gandham

Received: 16 January 2023  
Revised: 27 February 2023  
Accepted: 6 March 2023  
Published: 11 March 2023



**Copyright:** © 2023 by the authors. Licensee MDPI, Basel, Switzerland. This article is an open access article distributed under the terms and conditions of the Creative Commons Attribution (CC BY) license (<https://creativecommons.org/licenses/by/4.0/>).

## 1. Introduction

The UK civil nuclear waste inventory comprises a significant quantity (~140 teHM) of separated Pu [1]. The Nuclear Decommissioning Authority (NDA) supports the UK Government in identifying a long-term strategy that places this material beyond reach. Two high level options have been identified, including (1) conversion of PuO<sub>2</sub> into a (U,Pu)O<sub>2</sub> mixed oxide (MOX) fuel for burning in the existing fleet of light water reactors (LWRs) and (2) chemical immobilisation of the inventory into a suitable waste form prior to geological disposal [2,3]. The design requirements for waste forms containing a large proportion of actinides necessitate high aqueous durability and radiation stability and, as such, a large suite of waste form development trials have identified that synthetic derivatives of zirconolite (CaZrTi<sub>2</sub>O<sub>7</sub>) and pyrochlore (Gd<sub>2</sub>Ti<sub>2</sub>O<sub>7</sub>) structures are candidate host phases [4,5].

Zirconolite (CaZrTi<sub>2</sub>O<sub>7</sub>) acts as the primary actinide bearing phase in the SYNROC (SYNthetic ROCK) titanate waste form, present alongside perovskite (CaTiO<sub>3</sub>), hollandite (BaAl<sub>2</sub>Ti<sub>6</sub>O<sub>16</sub>) and rutile (TiO<sub>2</sub>) [6–8]. Zirconolite is best described as an anion-deficient fluorite superstructure and is closely related to the pyrochlore structure, with the general formula A<sub>2</sub>B<sub>2</sub>O<sub>7</sub> [9]. On the basis of the existence of naturally occurring mineral specimens with high quantities of retained actinides (namely U and Th); an affinity for extensive solid solution with REE<sup>3+</sup>, An<sup>3+/4+</sup> and transition metals (Al<sup>3+</sup>, Fe<sup>3+</sup>, Cr<sup>3+</sup>); high aqueous durability in laboratory trials; and moderate radiation stability, zirconolite is considered to be a candidate host phase for Pu. The ideal zirconolite-2M phase (monoclinic) is one of several polytype structures that have been characterised and comprises CaO<sub>8</sub> (eight-fold coordination), ZrO<sub>7</sub> (seven-fold coordination) and hexagonal tungsten bronze (HTB)

motifs with  $\text{TiO}_5$  (five-fold; 50% occupied) and two  $\text{TiO}_6$  (six-fold) layers. By extensive doping on the  $\text{Ca}^{2+}$  and/or the  $\text{Zr}^{4+}$  site(s), or varying the sintering environment, it is possible to stabilise a variety of polytype structures, characterised by changes in unit cell symmetry and variation of the stacking sequence of adjacent Ca/Zr and Ti polyhedral layers; examples include 3T, 4M or 3O [10–12]. The dual-site substitution of lanthanides and actinides (e.g.,  $\text{Pu}^{4+}$ ), i.e.,  $\text{Ca}^{2+}$  and  $\text{Zr}^{4+}$ , can be achieved with the incorporation of a lower valence charge compensator ( $\text{Fe}^{3+}$ ,  $\text{Al}^{3+}$ , etc.) within the  $\text{Ti}^{4+}$  site to maintain charge balance for the structure [13,14]. The dual substitution of the surrogate actinide fraction between the Ca and Zr sites can allow for a higher waste loading of  $\text{PuO}_2$  within and is the current baseline formulation investigated in the UK. This could feasibly lead to fewer waste packages and lower waste management costs, and reduced space requirements in a geological disposal facility [15]. A key design requirement for waste forms containing a considerable actinide fraction is the ability to co-incorporate a suitable inventory of neutron absorbing additive (typically Gd and/or Hf) to reduce the neutron flux in the disposal environment. Zirconolite has demonstrated high solubility of Gd and Hf across various solid solutions, e.g.,  $\text{Ca}_{1-x}\text{Gd}_x\text{ZrTi}_{2-x}\text{Al}_x\text{O}_7$  and  $\text{CaZr}_{1-x}\text{Hf}_x\text{Ti}_2\text{O}_7$  [16–18].

Hot isostatic pressing (HIP) is a potential technology for the processing and consolidation of zirconolite waste forms and offers several advantages over a conventional approach of cold uniaxial pressure prior to sintering, including access to lower process temperatures, high waste loading and improved accountability of fissile content within waste packages, volume reduction, improved handling and storage properties and reduced generation of secondary wastes products [19]. The simultaneous application of high temperature and pressure to a powder body within a hermetically sealed canister promotes the formation of high density ceramics by reducing porosity via compaction [20,21]. To demonstrate the feasibility of this approach for the immobilisation of Pu in a ceramic waste form, it is necessary to further optimise the feedstock properties to improve the quality of the final product [9,21].

Hence, the aim of the current work was to investigate the effect of wet planetary ball milling parameters on the quality of the  $(\text{Ca}_{0.783}\text{Gd}_{0.017}\text{Ce}_{0.2})(\text{Zr}_{0.883}\text{Gd}_{0.017}\text{Ce}_{0.1})(\text{Ti}_{1.6}\text{Al}_{0.4})\text{O}_7$  waste form processed by laboratory scale HIP. During initial studies, unincorporated  $\text{CeO}_2$  was observed, which was an undesirable minor phase. Therefore, the quality of the product was evaluated against the presence of unincorporated  $\text{CeO}_2$  (included as the  $\text{PuO}_2$  surrogate) and preclusion of detrimental secondary phases (e.g., perovskite). We here present the results of a range of milling parameters on the general features of the final HIPed product.

## 2. Experimental Method

### 2.1. Sample Preparation

The zirconolite formulation  $(\text{Ca}_{0.783}\text{Gd}_{0.017}\text{Ce}_{0.2})(\text{Zr}_{0.883}\text{Gd}_{0.017}\text{Ce}_{0.1})(\text{Ti}_{1.6}\text{Al}_{0.4})\text{O}_7$  was batched from a mixture of oxide precursors,  $\text{CaTiO}_3$ ,  $\text{ZrO}_2$ ,  $\text{TiO}_2$ ,  $\text{CeO}_2$ ,  $\text{Gd}_2\text{O}_3$  and  $\text{Al}_2\text{O}_3$  (Sigma Aldrich, <99.9% trace metals basis) to yield a total batch size of 70 g, adding 50% (*v/v*) isopropanol and water as a milling carrier fluid. Ball milling of the component oxides was performed using a Fritsch Pulverisette 7 planetary mill with a Fritsch  $\text{ZrO}_2$  milling jar and 3 mm Y- $\text{ZrO}_2$  stabilised media. To investigate the effect of milling time and reagent quality on the properties of the zirconolite product, a series of parameters were trialled using a fixed milling speed of 400 rpm (Table 1). Immediately post-milling, the slurry of each composition was dried at 90 °C overnight to evaporate excess solvent prior to sieving to separate milling media using a 212  $\mu\text{m}$  mesh. The dried powders were packed into the walls of a 304 stainless steel HIP canister under uniaxial pressure. The lids of each canister were welded on and qualified by heating to 300 °C until an internal pressure of <50 mTorr was achieved. The evacuation tubes were crimped and welded to qualify the canister as hermetically sealed. The sealed HIP canisters were placed into the AIP 630-H HIP unit in the HADES facility [22] with a programmed thermal/pressure cycle targeting 103 MPa and 1320 °C for 4 h (at heating and cooling rates of 10 °C  $\text{min}^{-1}$ ).

**Table 1.** A summary of investigated milling parameters.

Sample	Milling Parameters at 400 rpm
A	40 min with the direction reversed at a 20 min interval
B	60 min with the direction reversed at 20 min intervals
C	120 min with the direction reversed at 20 min intervals (20 min break after 1 h)
D	Pre-milled CeO <sub>2</sub> added; 20 min with the direction reversed at 10 min intervals, and then 60 min with the direction reversed at 20 min intervals
E	60 min with the direction reversed at 20 min intervals, using CeO <sub>2</sub> with a finer particle size (<5 μm)

## 2.2. Sample Characterisation

Each HIPed canister was sectioned to allow removal of the bulk zirconolite material for analysis. A fragment of material was extracted and ground to powder for X-ray diffraction analysis, performed using a Bruker D2 Phaser desktop diffractometer. The instrument utilised a Cu K $\alpha$  radiation source (1.5418 Å) operating in reflection mode, fitted with a Ni filter and Lynxeye position sensitive detector; data were collected in the interval  $5^\circ \leq 2\theta \leq 80^\circ$  with a step size of  $0.02^\circ$  and time per step of 1 s. Rietveld analysis of the powder diffraction profile was performed to approximate the relative quantity of each indexed phase and extract unit cell parameters; this was achieved using the GSAS software package with the EXPGUI interface [23].

To prepare materials for scanning electron microscopy (SEM) analysis, each HIPed canister was sectioned using an Isomet 1000 precision sectioning saw to obtain a flat slice that was mounted in cold setting epoxy resin. The face of each resin mount was polished to a 1 μm optical finish using a series of SiC grinding papers and diamond suspensions. All samples were carbon coated prior to analysis to prevent charge build-up on the surface. Backscattered electron micrographs and compositional analyses were obtained using a Hitachi TM3030 SEM operating at 15 kV and a 7.5 ( $\pm$  0.5) mm working distance, fitted with a Bruker Quantax Energy Dispersive X-ray Spectrometer (EDX). The bulk density of samples was measured using the Archimedes' method by immersion in ethanol. Measurements were performed at room temperature and the average density was determined from five data points.

To determine the average oxidation state of Ce within the HIPed zirconolite product, Ce L<sub>3</sub> edge X-ray absorption near edge spectroscopy (XANES) data were collected at Beamline 6-BM (National Synchrotron Light Source II, Brookhaven National Laboratory). To prepare each specimen for analysis, a small aliquot of powder was dispersed in polyethylene glycol (PEG) and pressed into 13 mm disks of a depth corresponding to one absorption length. The incident synchrotron radiation was scanned across the Ce L<sub>3</sub> edge energy range (5723 eV) to obtain an absorption edge that could be used for diagnostic analysis of the Ce oxidation state; data were collected alongside a variety of reference compounds (CePO<sub>4</sub> and CeO<sub>2</sub>) representing Ce in different oxidation states and coordination environments. XANES data reduction and analysis was accomplished using the Athena software [24].

## 3. Results and Discussion

### 3.1. Phase Assemblage

Powder XRD analysis was performed to identify the structure and relative quantity of each phase formed in the HIPed products (Figure 1). Zirconolite-2M (PDF: 00-074-0669) and zirconolite-3T (PDF: 01-072-7510) polytypes were formed in all samples as the dominant phase, with reflections characteristic of each polytype clearly visible in each diffraction profile. In each sample, a secondary perovskite phase (PDF: 00-042-0423) was identified by a series of intense reflections, with the diagnostic (121) reflection at  $2\theta = 33.1^\circ$ . The lowest concentration of perovskite was observed in Sample B. Additionally, unincorporated CeO<sub>2</sub> was observed in all the initial studies, which was an undesirable minor phase; however, it was not in sufficient quantity to be detected by XRD.

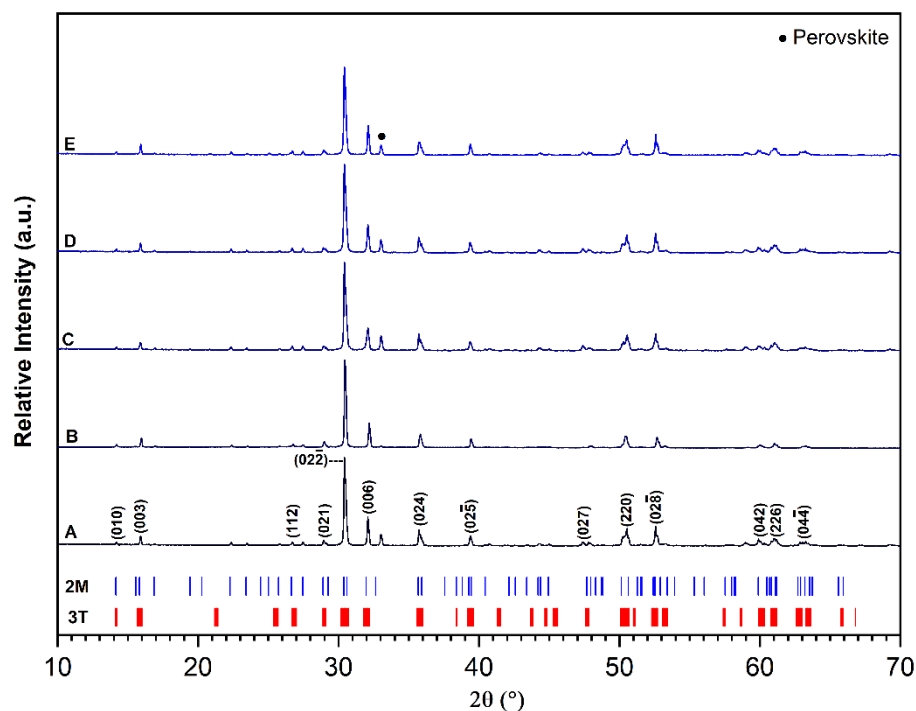


**Figure 1.** Powder XRD data for HIPed Samples A–E. Zirconolite-2M and -3T reflections are indexed with corresponding (hkl) values of zirconolite-3T.

Rietveld analysis of each powder diffraction profile was performed to determine the relative quantity of each phase (quantitative phase analysis, (QPA)) and unit cell (Table 2). The statistical indicators were as follows: R-factor,  $\chi^2$  values and  $R_{wp}$  are presented, where  $R_{wp}$  values below 10% represent reliable fits to the data. All samples (A–E) were composed of a mixture of zirconolite-2M and zirconolite-3T, with the former generally existing in a greater proportion. The highest yield of zirconolite-2M ratio was observed in Sample C at 85.61 (2) wt.%, alongside 4.75 (1) wt.% zirconolite-3T. The lowest zirconolite-2M proportion was 77.35 (4) wt.% for Sample B with 20.12 (1) wt.% zirconolite-3T. The accompanying quantity of the secondary perovskite phase varied from 11.72 (4) wt.% for Sample D (size reduced  $\text{CeO}_2$ ) and 2.65 (1) wt.% for the sample B (60 min mill) as the highest and lowest wt all of the batched  $\text{CeO}_2$  was successfully immobilised; thus, each HIPed sample was considered effective as a  $\text{PuO}_2$  host irrespective of milling conditions. However, the phase assemblage best suited to yield a single zirconolite waste form appeared to be Sample B (60 min mill) from the point of view that perovskite formation should be minimised as it is known to uptake  $\text{Pu}^{3+/4+}$  and have a lower durability than zirconolite [25].

**Table 2.** The weight ratio of phases and  $R_{wp}$ , R and  $\chi^2$  values of Samples A–E.

Sample	Zirc-2M (%)	Zirc-3T (%)	Perovskite (%)	$R_{wp}$	R	$\chi^2$
A	77.35(4)	12.75(1)	9.90(1)	9.16	7.04	3.92
B	77.23(4)	20.12(1)	2.65(1)	11.62	8.93	4.84
C	85.61(2)	4.75(1)	9.64(4)	8.69	6.74	3.85
D	78.16(4)	10.12(1)	11.72(4)	8.38	6.49	3.96
E	80.61(3)	11.50(1)	7.89(4)	9.16	7.05	4.17

The unit cell parameters for the obtained zirconolite-2M portion of the phase assemblages were calculated by the Rietveld method for each sample (Table 3). The unit cell dimensions for stoichiometric  $\text{CaZrTi}_2\text{O}_7$  were taken from Whittle et al. [26]. There was no discernible trend observed by varying the milling parameters.

**Table 3.** The unit cell parameters of zirconolite-2M formed in Samples A–E [26].

Sample	a (Å)	b (Å)	c (Å)	$\beta$ (°)	Vol (Å <sup>3</sup> )
CaZrTi <sub>2</sub> O <sub>7</sub> [26]	12.4430(1)	7.2729(1)	11.3809(1)	100.56(1)	1012.48(2)
A	12.490(1)	7.264(6)	11.3561(9)	100.71(1)	1012.5(1)
B	12.521(2)	7.252(1)	11.329(2)	100.57(2)	1010.6(2)
C	12.492(1)	7.2671(6)	11.3575(8)	100.70(1)	1013.1(1)
D	12.484(2)	7.2652(8)	11.359(1)	100.68(1)	1012.4(2)
E	12.496(1)	7.2660(8)	11.351(1)	100.72(1)	1012.7(2)

### 3.2. Microstructure Analysis

The quality of the HIPed product was also evaluated by observations of the microstructure (Figure 2). For Sample A, both zirconolite-2M and -3T are represented as a mid-grey area without any other phase detectable. The microstructure of Sample A appears different to the remaining sample suite, with a notably higher degree of visible porosity. As this sample was produced using the lowest milling duration, it may signify less efficient compaction and sintering pathways, therefore opposing densification during HIPing. For Sample B, zirconolite polytypes are represented by a mid-grey bulk matrix; however, the microstructure is clearly interspersed with an additional phase identified by small light-contrast particulates, confirmed by EDS analysis as CeO<sub>2</sub>. Reflections corresponding to CeO<sub>2</sub> were not identified in the XRD or QPA; thus, it was concluded that the concentration of unincorporated CeO<sub>2</sub> was likely below 2 wt.% in this sample. Sample D contained zirconolite as the major phase identified by the mid-grey area, with the secondary perovskite phase clearly identified as dark-grey regions; additionally, unincorporated Al<sub>2</sub>O<sub>3</sub> (black areas) were also identified by EDS analysis, suggesting a degree of phase instability in this sample (size reduced CeO<sub>2</sub>). However, unincorporated Al<sub>2</sub>O<sub>3</sub> was not determined by QPA analysis due to the low concentration (<2 wt.%). For Samples C and E, two different microstructures were identified across the sample as highlighted in Figure 2. The SEM images of C.1 (Figure 3) and E.1 represent the homogenous zirconolite formation (extracted from the bulk matrix), whereas C.2 (Figure 4) and E.2 evidence Ce-containing perovskite. The perovskite determined via XRD and QPA analysis (9.64 (4) wt.% and 7.89 (4) wt.% for Samples C and E, respectively) corroborated these images, as these analyses were completed by using the whole HIPed sample slice and highlight variability in phase distribution across the diameter of the HIP canister. As a result, Sample B had a more homogenous zirconolite structure without perovskite formation than the other samples.

Semi-quantitative compositional analysis was performed across 10 areas across the zirconolite-2M/3T phases and compared to the targeted composition (Table 4). According to the nominal (Ca<sub>0.783</sub>Gd<sub>0.017</sub>Ce<sub>0.2</sub>)(Zr<sub>0.883</sub>Gd<sub>0.017</sub>Ce<sub>0.1</sub>)(Ti<sub>1.6</sub>Al<sub>0.4</sub>O<sub>7</sub>) formulations, the compounds formed were close to the desired composition, evidencing successful Ce, Gd and Al incorporations. The variation of the Ce ratio was rationalised by the presence of Ce-rich perovskite phases which were clearly observed on SEM images.

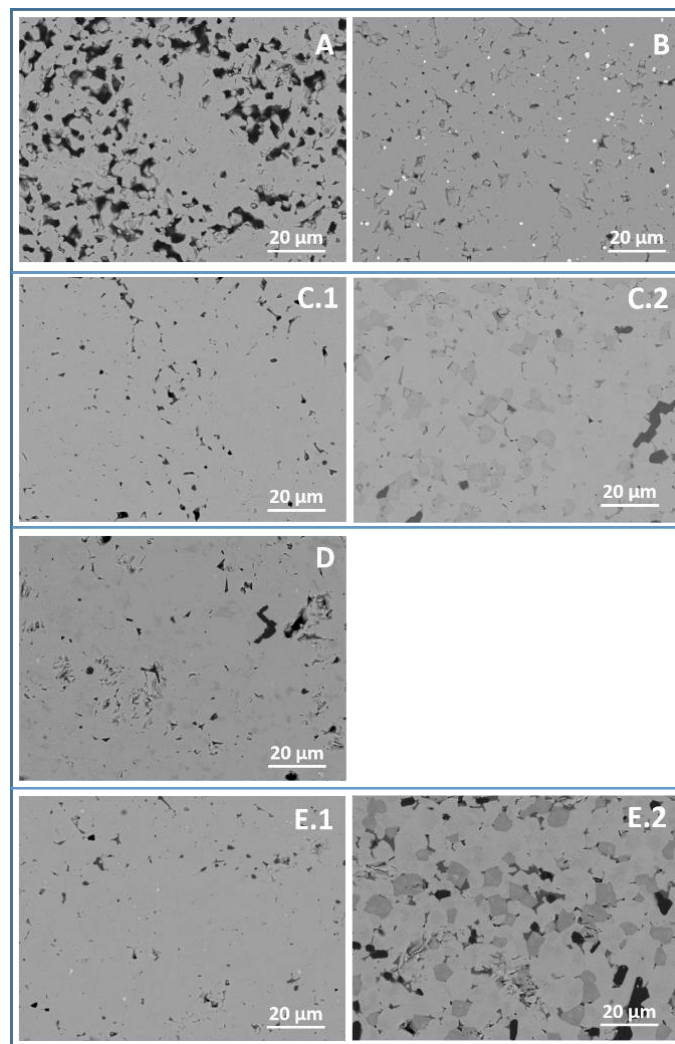


**Figure 2.** SEM micrographs of HIPed samples (A–E) prepared with different milling parameters at 400 rpm. Two areas are displayed for Samples C and E, labelled as C.1 and C.2 respectively.

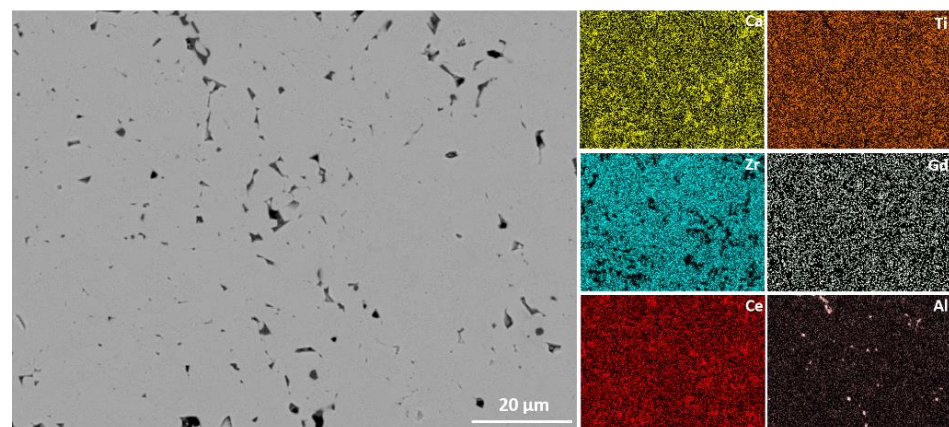


**Figure 3.** SEM micrographs of HIPed Sample C.1 at 400 rpm during 120 min.

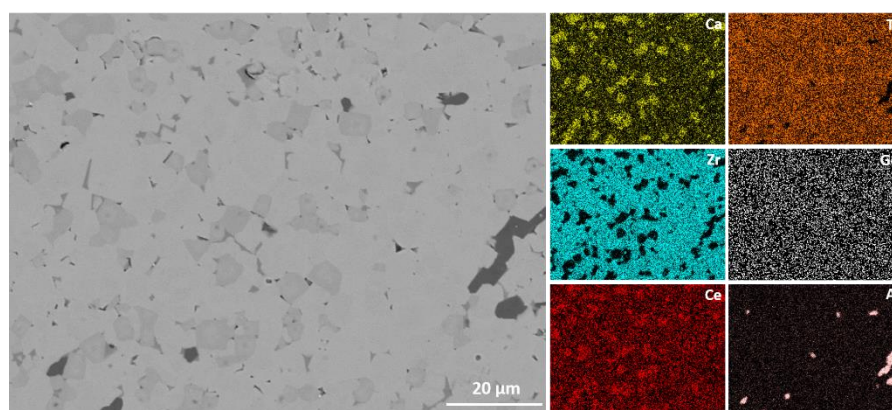


**Figure 4.** SEM micrographs of HIPed Sample C.2 at 400 rpm during 120 min.

**Table 4.** Experimental compositions of different samples (Theoretical composition:  $(\text{Ca}_{0.783}\text{Gd}_{0.017}\text{Ce}_{0.2})(\text{Zr}_{0.883}\text{Gd}_{0.017}\text{Ce}_{0.1})(\text{Ti}_{1.6}\text{Al}_{0.4})\text{O}_7$ ).

Sample	Experimental Formulation
A	$(\text{Ca}_{0.83(4)}\text{Gd}_{0.013(9)}\text{Ce}_{0.20(2)})(\text{Zr}_{0.76(5)}\text{Gd}_{0.013(9)}\text{Ce}_{0.10(1)})(\text{Ti}_{1.72(4)}\text{Al}_{0.33(4)})\text{O}_7$
B	$(\text{Ca}_{0.78(4)}\text{Gd}_{0.007(3)}\text{Ce}_{0.14(2)})(\text{Zr}_{0.95(7)}\text{Gd}_{0.007(3)}\text{Ce}_{0.07(1)})(\text{Ti}_{1.62(6)}\text{Al}_{0.40(4)})\text{O}_7$
C	$(\text{Ca}_{0.81(7)}\text{Gd}_{0.011(6)}\text{Ce}_{0.14(2)})(\text{Zr}_{0.81(9)}\text{Gd}_{0.011(6)}\text{Ce}_{0.07(1)})(\text{Ti}_{1.54(5)}\text{Al}_{0.32(3)})\text{O}_7$
D	$(\text{Ca}_{0.84(8)}\text{Gd}_{0.01(3)}\text{Ce}_{0.14(2)})(\text{Zr}_{0.94(10)}\text{Gd}_{0.01(3)}\text{Ce}_{0.07(1)})(\text{Ti}_{1.60(9)}\text{Al}_{0.37(4)})\text{O}_7$
E	$(\text{Ca}_{0.80(5)}\text{Gd}_{0.013(6)}\text{Ce}_{0.17(2)})(\text{Zr}_{0.86(8)}\text{Gd}_{0.013(6)}\text{Ce}_{0.08(1)})(\text{Ti}_{1.67(5)}\text{Al}_{0.37(3)})\text{O}_7$

The measured densities of bulk ceramic materials are listed in Table 5. When compared with the theoretical density of stoichiometric  $\text{CaZrTi}_2\text{O}_7$  ( $4.44 \text{ g/cm}^3$ ), it was clear that the HIPed products generally formed with a higher relative density between approximately  $4.64$  and  $4.68 \text{ g/cm}^3$  attributed to the incorporation of heavier cations (Ce, Gd) within the structure [25]. The density of Sample A was measured as  $4.18(2) \text{ g/cm}^3$ ; however, this was consistent with the porous microstructure of the material observed by SEM.

**Table 5.** Densities of Samples A–E.

Sample	Density ( $\text{g cm}^{-3}$ )
A	4.18(2)
B	4.64(3)
C	4.64(2)
D	4.68(2)
E	4.67(2)

### 3.3. Oxidation State and Local Environment of Ce

Ce  $L_3$ -edge XANES analysis was performed to investigate the average Ce oxidation state in the HIPed materials and determine whether there was a tangible relationship between milling parameters and prevailing Ce oxidation state. The data were acquired alongside  $\text{CeO}_2$  and  $\text{CePO}_4$ , acting as reference compounds containing  $\text{Ce}^{4+}$  in eight-fold coordination and  $\text{Ce}^{3+}$  in nine-fold coordination, respectively (Figure 5). The white line for the  $\text{CeO}_2$  compound has a doublet of two overlapping peaks, whereas the white line of  $\text{CePO}_4$  comprises a single intense peak, providing easily distinguishable characteristics for determining the Ce oxidation state [27]. The XANES data revealed that for each sample (A–E), Ce occurred as mixed  $\text{Ce}^{4+}/\text{Ce}^{3+}$ . The relative proportions of  $\text{Ce}^{4+}/\text{Ce}^{3+}$  were determined by linear combination fitting using the  $\text{CeO}_2$  and  $\text{CePO}_4$  spectra (Table 6) [24]. The greatest  $\text{Ce}^{4+}$  content was produced in Sample A, at approximately 79 (1)%, whereas in samples C, D and E,  $\text{Ce}^{4+}$  was present at approximately 30%. These data imply that a longer milling duration (120 min) and reduction in the initial  $\text{CeO}_2$  primary particle size may lead

to greater proportion of  $\text{Ce}^{3+}$  in the HIPed product.  $\text{Ce}^{3+}$  can be readily incorporated into a Ce-bearing perovskite phase, and with the exception of sample A, the samples with the highest perovskite concentration were clearly correlated with the highest proportion of  $\text{Ce}^{3+}$ . Precluding the formation of additional perovskite phases is beneficial, as this phase is known to lower the overall durability of zirconolite-rich waste form compositions when present, even in low quantities [28]. As the XANES technique is probing the global Ce oxidation state, some of the signal will represent Ce present in Ce-bearing perovskite and unincorporated  $\text{CeO}_2$  (demonstrated in the SEM image of sample B), which should be taken into account when assessing the data. As a result of XANES analysis, the optimum milling parameter could be determined as 40 min (Sample A) to provide the highest  $\text{Ce}^{4+}$  ratio.

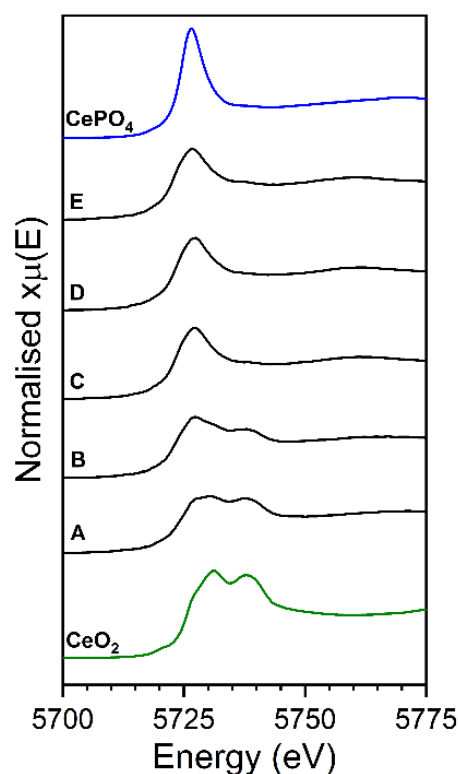


**Figure 5.** Ce  $L_3$ -edge XANES spectra for Samples A–E, alongside  $\text{CeO}_2$  and  $\text{CePO}_4$  reference compounds.

**Table 6.** Linear combination fitting of Ce  $L_3$ -edge XANES data.

Sample	$\text{Ce}^{4+}\text{O}_2$ (%)	$\text{Ce}^{3+}\text{PO}_4$ (%)	R-Factor
A	79(1)	21(3)	0.02
B	60(2)	40(4)	0.04
C	31(3)	69(4)	0.10
D	30(3)	70(4)	0.10
E	32(3)	68(4)	0.10

#### 4. Conclusions

A viable option for placing the UK civil Pu inventory beyond reach is immobilisation in a zirconolite matrix, fabricated by a campaign of hot isostatic pressing. Ongoing waste form development efforts are seeking to optimise processing parameters associated with the HIP process, including thermal/pressure cycles and milling parameters in preparation of the actinide-loaded feedstock. Moreover, it is necessary to establish the solubility of charge balancing cations (Al, Fe) and neutron absorbing additives (Gd, Hf) within zirconolite-structured materials. In the present work, a series of milling parameters were

trialled to optimise the phase assemblage and microstructure of a zirconolite with the nominal composition  $(\text{Ca}_{0.783}\text{Gd}_{0.017}\text{Ce}_{0.2})(\text{Zr}_{0.883}\text{Gd}_{0.017}\text{Ce}_{0.1})(\text{Ti}_{1.6}\text{Al}_{0.4})\text{O}_7$ . A series of feedstocks targeting this formulation were prepared by a variety of milling routes at 400 rpm, aiming to establish the influence of milling time and the primary particle size of the actinide surrogate ( $\text{CeO}_2$ ) on the overall quality of the HIPed product, processed 1320 °C for 4 h under 103 MPa isostatic pressure. XRD analysis revealed that a combination of zirconolite-2M and -3T polytypes constituted the major phases in the waste form; however, a perovskite phase remained present in all samples at varying concentrations. Rietveld analysis of the powder diffraction data indicated that the highest yield of zirconolite-2M was 85.61 (2) wt.% in Sample C, whereas the sample B had a greater proportion of the zirconolite-3T phase; additionally, the lowest perovskite concentration, estimated at 2.65 (1) wt.%. SEM data, confirmed that zirconolite polytypes constituted the major phase(s) for all samples. For Sample B, unincorporated  $\text{CeO}_2$  was observed in the microstructure; Samples C and E evidenced two different microstructures observed on the same sample surface. Ce-rich perovskite phases were clearly identified by SEM and XRD analysis; moreover, with increased perovskite, unincorporated  $\text{Al}_2\text{O}_3$  was also observed. The greatest concentration of  $\text{Ce}^{4+}$  was obtained in Sample A, whereas a minimum  $\text{Ce}^{4+}$  concentration of approximately 31 (3)% was obtained in Sample C, with a marked increase in milling duration. The evaluation of the milling time revealed that the optimum milling parameter was 60 min based on a homogenous zirconolite microstructure with less porosity and the lowest perovskite formation. In addition, the pre-milling of the  $\text{CeO}_2$  feedstock promoted increased perovskite formation and a larger relative  $\text{Ce}^{3+}$  fraction. Consequently, the optimum milling parameter was indicated as 60 min with the direction reversed at 20 min intervals for future HIP studies.

**Author Contributions:** Conceptualization, M.K.; Methodology, M.K.; Formal analysis, M.K., L.J.G., L.R.B., M.C.S., N.C.H. and C.L.C.; Investigation, M.K.; Writing—original draft, M.K.; Writing—review & editing, L.J.G., L.R.B., M.C.S. and C.L.C.; Supervision, M.C.S., N.C.H. and C.L.C.; Funding acquisition, N.C.H. and C.L.C. All authors have read and agreed to the published version of the manuscript.

**Funding:** CLC is grateful to EPSRC for the award of an Early Career Fellowship under grant reference EP/N017374/1. NCH wishes to acknowledge the Royal Academy of Engineering and the NDA for funding and EPSRC for part support under grant references EP/S032959/1, EP/P013600/1 and EP/N017617/1. This research utilised the HADES/MIDAS facility at the University of Sheffield, established with financial support from EPSRC and BEIS, under grant EP/T011424/1. MK is grateful to the Ministry of Education of the Republic of Turkey for funding her PhD scholarship at the University of Sheffield. We gratefully acknowledge EPSRC for partial support under grant reference EP/S01019X/1 for the TRANSCEND (Transformative Science and Engineering for Nuclear Decommissioning) facility. This research used beamline 6-BM of the National Synchrotron Light Source II, a U.S. Department of Energy (DOE) Office of Science User Facility operated for the DOE office of Science by Brookhaven National Laboratory under Contract No. DE-SC0012704; we gratefully acknowledge Bruce Ravel.

**Data Availability Statement:** The raw data that support these findings cannot be shared at this time as the data also form part of an ongoing study.

**Conflicts of Interest:** The authors declare that they have no known competing financial interests or personal relationships that could have appeared to influence the work reported in this paper.

## References

1. Nuclear Decommissioning Authority. Progress on Plutonium Consolidation, Storage and Disposition. 2019. Available online: [https://assets.publishing.service.gov.uk/government/uploads/system/uploads/attachment\\_data/file/791046/Progress\\_on\\_Plutonium.pdf](https://assets.publishing.service.gov.uk/government/uploads/system/uploads/attachment_data/file/791046/Progress_on_Plutonium.pdf) (accessed on 15 January 2023).
2. Hyatt, N.C. Plutonium management policy in the United Kingdom: The need for a dual track strategy. *Energy Policy* **2017**, *101*, 303–309. [CrossRef]
3. Hyatt, N.C. Safe management of the UK separated plutonium inventory: A challenge of materials degradation. *NPJ Mater. Degrad.* **2020**, *4*, 28. [CrossRef]

4. Ewing, R.C.; Weber, W.J.; Lian, J. Nuclear waste disposal—Pyrochlore ( $A_2B_2O_7$ ): Nuclear waste form for the immobilization of plutonium and “minor” actinides. *J. Appl. Phys.* **2004**, *95*, 5949–5971. [[CrossRef](#)]
5. Weber, W.J.; Ewing, R.C.; Catlow, C.R.A.; de la Rubia, T.D.; Hobbs, L.W.; Kinoshita, C.; Matzke, H.; Motta, A.T.; Nastasi, M.; Salje, E.K.H.; et al. Radiation effects in crystalline ceramics for the immobilization of high-level nuclear waste and plutonium. *J. Mater. Res.* **1998**, *13*, 1434–1484. [[CrossRef](#)]
6. Gregg, D.J.; Vance, E.R. Synroc tailored waste forms for actinide immobilization. *Radiochim. Acta* **2017**, *105*, 907–925. [[CrossRef](#)]
7. Vance, E.R.; Stewart, M.W.A.; Moricca, S.A. Progress at ANSTO on SYNROC. *J. Aust. Ceram. Soc.* **2014**, *50*, 38–48.
8. Jantzen, C.M.; Ojovan, M.I. On Selection of Matrix (Wasteform) Material for Higher Activity Nuclear Waste Immobilization (Review). *Russ. J. Inorg. Chem.* **2019**, *64*, 1611–1624. [[CrossRef](#)]
9. Gregg, D.J.; Farzana, R.; Dayal, P.; Holmes, R.; Triani, G. Synroc technology: Perspectives and current status (Review). *J. Am. Ceram. Soc.* **2020**, *103*, 5424–5441. [[CrossRef](#)]
10. Lumpkin, G.R. Ceramic Waste Forms for Actinides. *Elements* **2006**, *2*, 365–372. [[CrossRef](#)]
11. Begg, B.D.; Vance, E.R.; Hunter, B.A.; Hanna, J.V. Zirconolite transformation under reducing conditions. *J. Mater. Res.* **1998**, *13*, 3181–3190. [[CrossRef](#)]
12. Zhang, Y.; Gregg, D.J.; Kong, L.; Jovanovich, M.; Triani, G. Zirconolite glass-ceramics for plutonium immobilization: The effects of processing redox conditions on charge compensation and durability. *J. Nucl. Mater.* **2017**, *490*, 238–241. [[CrossRef](#)]
13. Aldean, I.; Sun, S.-K.; Wilkins, M.C.D.; Gardner, L.J.; Mason, A.R.; Stennett, M.C.; Corkhill, C.L.; Hyatt, N.C.; Blackburn, L.R. Synthesis and characterisation of Ce-doped zirconolite  $Ca_{0.80}Ce_{0.20}ZrTi_{1.60}M_{0.40}O_7$  ( $M = Fe, Al$ ) formed by reactive spark plasma sintering (RSPS). *MRS Adv.* **2022**, *7*, 75–80. [[CrossRef](#)]
14. Lumpkin, G.; Whittle, K.; Howard, C.; Zhang, Z.; Berry, F.; Oates, G.; Williams, C.; Zaitsev, A. Crystal Chemistry and Cation Ordering in Zirconolite 2M. *MRS Online Proc. Libr.* **2006**, *932*, 53. [[CrossRef](#)]
15. Zhang, Y.; Kong, L.; Ionescu, M.; Gregg, D.J. Current advances on titanate glass-ceramic composite materials as waste forms for actinide immobilization: A technical review. *J. Eur. Ceram. Soc.* **2022**, *42*, 1852–1876. [[CrossRef](#)]
16. Yudinsev, S.V.; Stefanovsky, S.V.; Nikonov, B.S.; Nikol'Skii, M.S.; Livshits, T.S. Potential matrices for immobilization of the rare earth-actinide fraction of high-level waste in the  $REE_2Zr_2O_7$ - $REE_2Ti_2O_7$  system. *Radiochemistry* **2015**, *57*, 187–199. [[CrossRef](#)]
17. Stefanovsky, S.V.; Troole, A.Y.; Lapina, M.I.; Nikonov, B.S.; Sivtsov, A.V.; Yudinsev, S.V. XRD, SEM and TEM Study of the Gd-Doped Zirconolites. *MRS Proc.* **2002**, *713*, 345–350. [[CrossRef](#)]
18. Zhang, K.; Yin, D.; He, Z.; Luo, B.; Zhang, H. Combustion synthesis of Hf-doped zirconolite-rich composite waste forms and the aqueous durability. *J. Adv. Ceram.* **2019**, *8*, 448–455. [[CrossRef](#)]
19. Gardner, L.J.; A Walling, S.; Hyatt, N.C. Hot isostatic pressing: Thermal treatment trials of inactive and radioactive simulant UK intermediate level waste. *IOP Conf. Ser. Mater. Sci. Eng.* **2020**, *818*, 012009. [[CrossRef](#)]
20. Thornber, S.M.; Heath, P.G.; Da Costa, G.P.; Stennett, M.C.; Hyatt, N.C. The effect of pre-treatment parameters on the quality of glass-ceramic wasteforms for plutonium immobilisation, consolidated by hot isostatic pressing. *J. Nucl. Mater.* **2017**, *485*, 253–261. [[CrossRef](#)]
21. Stewart, M.W.A.; Moricca, S.A.; Eddowes, T.; Zhang, Y.; Vance, E.R.; Lumpkin, G.R.; Carter, M.L.; Dowson, M.; James, M. The Use of Hot-Isostatic Pressing to Process Nuclear Waste Forms. In Proceedings of the ASME 2009 12th International Conference on Environmental Remediation and Radioactive Waste Management, Liverpool, UK, 11–15 October 2009; pp. 611–616. [[CrossRef](#)]
22. Hyatt, N.C.; Corkhill, C.L.; Stennett, M.C.; Hand, R.J.; Gardner, L.J.; Thorpe, C.L. The HADES Facility for High Activity Decommissioning Engineering & Science: Part of the UK National Nuclear User Facility. *IOP Conf. Series: Mater. Sci. Eng.* **2020**, *818*, 012022. [[CrossRef](#)]
23. Toby, B.H. *EXPGUI*, a graphical user interface for *GSAS*. *J. Appl. Crystallogr.* **2001**, *34*, 210–213. [[CrossRef](#)]
24. Ravel, B.; Newville, M. ATHENA, ARTEMIS, HEPHAESTUS: Data analysis for X-ray absorption spectroscopy using IFEFFIT. *J. Synchrotron Radiat.* **2005**, *12*, 537–541. [[CrossRef](#)]
25. Blackburn, L.R.; Bailey, D.J.; Sun, S.-K.; Gardner, L.J.; Stennett, M.C.; Corkhill, C.L.; Hyatt, N.C. Review of zirconolite crystal chemistry and aqueous durability. *Adv. Appl. Ceram.* **2021**, *120*, 69–83. [[CrossRef](#)]
26. Whittle, K.R.; Hyatt, N.; Smith, K.L.; Margiolaki, I.; Berry, F.J.; Knight, K.S.; Lumpkin, G.R. Combined neutron and X-ray diffraction determination of disorder in doped zirconolite-2M. *Am. Miner.* **2012**, *97*, 291–298. [[CrossRef](#)]
27. Blackburn, L.R.; Sun, S.; Gardner, L.J.; Maddrell, E.R.; Stennett, M.C.; Hyatt, N.C. A systematic investigation of the phase assemblage and microstructure of the zirconolite  $CaZr_{1-x}Ce_xTi_2O_7$  system. *J. Nucl. Mater.* **2020**, *535*, 152137. [[CrossRef](#)]
28. Blackburn, L.R.; Crawford, R.; Walling, S.A.; Gardner, L.J.; Cole, M.R.; Sun, S.-K.; Gausse, C.; Mason, A.R.; Stennett, M.C.; Maddrell, E.R.; et al. Influence of accessory phases and surrogate type on accelerated leaching of zirconolite waste forms. *NPJ Mater. Degrad.* **2021**, *5*, 1–11. [[CrossRef](#)]

**Disclaimer/Publisher's Note:** The statements, opinions and data contained in all publications are solely those of the individual author(s) and contributor(s) and not of MDPI and/or the editor(s). MDPI and/or the editor(s) disclaim responsibility for any injury to people or property resulting from any ideas, methods, instructions or products referred to in the content.